Interfacial charge separation and photovoltaic efficiency in Fe(ii)–carbene sensitized solar cells

Mariachiara Pastore, Thibaut Duchanois, Li Liu, Antonio Monari, Xavier Assfeld, Stefan Haacke, Philippe Gros

To cite this version:

Mariachiara Pastore, Thibaut Duchanois, Li Liu, Antonio Monari, Xavier Assfeld, et al.. Interfacial charge separation and photovoltaic efficiency in Fe(ii)–carbene sensitized solar cells. Physical Chemistry Chemical Physics, 2016, 18 (40), pp.28069-28081. 10.1039/C6CP05535D . hal-01812853

HAL Id: hal-01812853
https://hal.science/hal-01812853

Submitted on 6 Nov 2018

Interfacial charge separation and photovoltaic efficiency in Fe(II)-carbene sensitized solar cells

Mariachiara Pastore*[a], Thibaut Duchanois,[b] Li Liu,[c] Antonio Monari,[a] Xavier Assfeld,[a] Stefan Haacke,[c] Philippe C. Gros*[b]

[a] *Université de Lorraine & CNRS, SRSMC, TMS, , Boulevard des Aiguillettes, 54506 Vandoeuvre-lès-Nancy, France.*

[b] *Université de Lorraine & CNRS, SRSMC, HecRIn, Boulevard des Aiguillettes, 54506 Vandoeuvre-lès-Nancy, France.*

[c] Université de Strasbourg & CNRS, IPCMS & Labex NIE, Rue du Loess, 67034 Strasbourg Cedex, France.

E-mail: mariachiara.pastore@univ-lorraine.fr, philippe.gros@univ-lorraine.fr

ABSTRACT

The first combined theoretical and photovoltaic characterization of both homoleptic and heteroleptic Fe(II)-carbene sensitized photoanodes in working dye sensitized solar cells (DSSCs) has been performed. Three new heteroleptic Fe(II)-NHC dye sensitizers have been synthesized, characterized and tested. Despite an improved interfacial charge separation in comparison to the homoleptic compounds, the heteroleptic complexes did not show boosted photovoltaic performances. The ab initio quantitative analysis of the interfacial electron and hole transfers and the measured photovoltaic data clearly evidenced fast recombination reactions for heteroleptics, even associated to un unfavorable directional electron flow, and hence slower injection rates, in the case of homoleptics. Notably, quantum mechanics calculations revealed that deprotonation of the not anchored carboxylic function in the homoleptic complex can effectively accelerate the electron injection rate and completely suppress the electron recombination to the oxidized dye. This result suggests that introduction of strong electron-donating substituents on the not-anchored carbene ligand in heteroleptic complexes, in such a way of mimicking the electronic effects of the carboxylate functionality, should yield markedly improved interfacial charge generation properties. The present results, providing for the first time a detailed understanding of the interfacial electron transfers and photovoltaic characterization in Fe(II)-carbene sensitized solar cells, open the way to a rational molecular engineering of efficient iron-based dyes for photoelectrochemical applications.

KEYWORDS

Iron(II) complexes; dye-sensitized TiO_2; DFT; electron injection, electron recombination.

1. Introduction

Due to the continuous consumption of fossil fuels and the associated inexorable increase in environmental pollution, exploiting the solar energy to produce electricity,[1] or storing it into H_2 or alternative solar fuels,[2-4] represents one of the most compelling technological challenges. In this context, nanostructured dye-sensitized solar cells (DSSCs)[5-9] offer a valuable solution, at a comparable cost and, in principle, lower environmental impact, to traditional silicon-based photovoltaics. To date ruthenium polypyridyl complexes have been the most extensively studied dyes sensitizers with up to 11% conversion efficiency.[10-14] The remarkable success obtained by Ru(II) dyes when employed as photosensitizers or photocatalysts[15, 16] can be traced back to their high electron injection quantum yields,[15, 17-21] coming from the high values of the electron injection rates compared to the intrinsic long lifetimes (from tens to hundreds of nanoseconds) of metal to ligand charge transfer (MLCT) lowest excited states of isolated complexes. These MLCT states are indeed responsible of the electron injection into the semiconductor conduction band (CB). Electron injection is also favored by an efficient interfacial electron-hole separation and by their peculiar adsorption geometry.[21] The same properties minimize detrimental charge recombination back onto the sensitizer. However, despite its record efficiencies, in the view of large-scale solar energy production, ruthenium suffers from serious drawbacks, which potentially limit its widespread applicability, mainly related to its toxicity and scarcity. This has motivated continuous research efforts to develop valuable alternatives: cheap and easily tunable fully organic sensitizers on one side,[22, 23] and earth-abundant, less expensive and environmentally friendly d-block metal (for example iron and copper) complexes on the other side.[24-33] Despite an intense MLCT absorption, however, conventional Fe(II)-polypyridyl complexes are, unfortunately, characterized by an ultrafast (ca. 100 *fs*) deactivation to low-lying Metal Centered (MC) states, proceeding via the triplet ^{3}MC and ultimately populating the quintuplet $^5T_2$ state,[34-39] which impedes electron injection into the sensitized semiconductor.[40, 41] One of the most successful strategies employed to delay the deactivation of ^{1,3}MLCT to MC states consists in increasing the ligand field strength.[42-55] In particular, significant advances have been recently reported by the use of N-heterocyclic carbene (NHC),[47, 52-54, 56] where, as a consequence of the presence of the σ-donating carbene ligands, the metal-centered ^{3}MC and $^5T_2$ states are strongly destabilized, resulting in record ^{3}MLCT lifetimes of 16 and 26 ps,[54] for the **C2**[52] and **C4**[4] complexes (functionalized by carboxylic groups to be covalently grafted to the TiO_2 surface) shown in Figure 1.

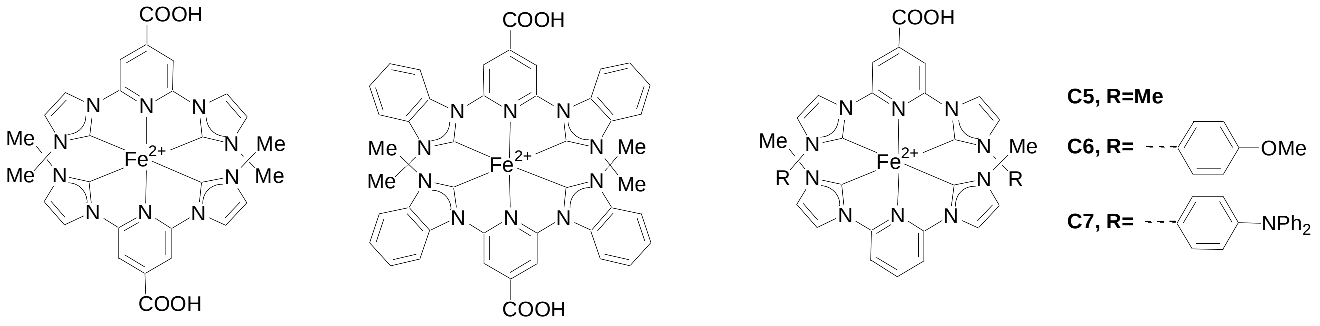

C2 **C4**

Figure 1. Chemical structures of the investigated iron complexes.

Besides the improved ^{1,3}MLCT lifetime, constituting the prerequisite for injecting electrons into the semiconductor's CB, the measured overall cell efficiency finally depends on the peculiar molecule/metal oxide interfacial properties (adsorption configuration, electronic coupling, charge generation, charge recombination etc…), which in turn can be reliably characterized by state-of-the-art first principle calculations.[57-60] In the last decade, indeed, quantum mechanical modeling of the isolated cell components[40, 44, 48, 52-54, 61-63] as well as of combined dye/semiconductor systems[39, 43, 51, 57, 64-68] have been shown to successfully support the experimental research by providing an atomistic understanding of the fundamental chemical and physical processes governing the cell functioning and its performances**.**

As a matter of fact, the first photovoltaic characterization of the Fe(II)-NHC complex **C2** (Figure 1) was reported by some of us in Ref. [52], with the first realization of a potentially exploitable iron-based DSSCs. **C2**-based devices revealed, however, low current generation and photovoltage, finally resulting in a weak power conversion efficiencies. Interestingly, a subsequent work by Wärnmark and co-workers[49] claimed a record injection efficiency, almost unitary, for the same complex, suggesting that the vibrationally relaxed and long-lived ^{3}MLCT might be responsible for this exceptionally high injection yield. Density functional theory (DFT) calculations were also reported by the authors[49] to rationalize the experimental findings, although their computations were limited to the energy level alignment calculated for the isolated dye and TiO_2 anatase slab, that is the electronic structure of the dye/TiO_2 interface was not considered. The reported high injection yield and low photovoltaic performances in working DSSCs, clearly, pose intriguing questions related to the efficiency of the forward and back interfacial electron transfer processes, whose interplay determines the final cell performance. This issue was partially tackled by a second recent computational contribution put forward by the same authors:[51] here, along with the electronic and excited state properties of isolated Fe(II)-NHC complexes, the structure of the dye/TiO_2 interface was also investigated, at least for a prototypical heteroleptic analogous of the original **C2** complex (**C5** in Figure 1). Analysis of the projected dye and TiO_2 density of states (PDOS) at the interface revealed that energetics and nature of the highest occupied and lowest unoccupied molecular orbitals (HOMOs and LUMOs) should allow efficient (ca. 100 *fs*) electron injection from both hot and thermally relaxed dye's ^{3}MLCT excited states to the semiconductor conduction band.[51] As pointed out by Galoppini,[69] a number of open issues, however, still remain toward the development of efficient iron-based DSSCs. The peculiar interfacial properties of the homoleptic **C2** complex showing conflicting unitary injection yield[49] and extremely low photovoltaic efficiency have not been yet elucidated, as well as the impact on the solar cell performances of possible structural modifications of the NHC ligands core (**C4** in Figure 1). Moreover, calculations suggest that the heteroleptic complexes potentially have the desired interfacial energetic and electronic coupling to efficiently sensitize the TiO_2 surface,[51] but their synthesis and applications in working DSSCs has not reported up to now.

Thus, with the aim of providing an unified and fundamental understanding of the interfacial charge generation and sensitization properties of Fe(II)-carbene complexes in working DSSCs, we report a quantitative analysis based on high-level DFT calculations on realistic models of the relevant interfacial electron transfers as well as, to the best of our knowledge, the first photovoltaic application of new homoleptic (C4 in Figure 1) and heteroleptic Fe(II)-NHC complexes (**C5**, **C6** and **C7** Figure 1).

Our findings definitely show that for the homoleptic complexes, although electron injection from the lowest energy MLCT dye's excited state is energetically favored, in the surface-grafted sensitizer the topology of the lowest-energy MLCT state does not allow electronic coupling with the surface and hence an efficient electron injection mechanism. Operational conditions favoring deprotonation of the not-coordinated carboxylic group might however invert the stability of the two lowest MLCT states and allow, at a certain extent, electron injection into the semiconductor. On the other hand, heterolpetic sensitizers, despite being characterized by the desired charge flow toward the TiO_2 surface in the lowest MLCT state, still present lower injection rates when compared to the best performing Ru(II)-polypyridyl and, as a matter of fact, do not yield improved photovoltaic performances. Besides the design of Fe(II) complexes endowed with long-lived ^{3}MLCT states strongly coupled with the semiconductor CB states, the present results, in line with the fast hole/electron recombination reactions observed by Wärnmark and co-workers,[49] indicate that the main obstacle to the development of efficient Fe(II)-based dye sensitizers is represented by the high favored recombination pathways with both the oxidized dye and the redox mediator.

2. Methods and Models

2.1 Synthesis of dyes

C2 and **C4** have been prepared according to Ref.[52] and [54] respectively. The preparation of heteroleptic complexes **C5**, **C6** and **C7** is described in Supporting Information.

2.2 DSSC fabrication and photovoltaic measurements.

The fluorine-doped tin oxide (FTO) glass plates (TEC Glass-TEC 8, solar 2.3 mm thickness), TiO_2 paste, electrolyte (AN50) and Pt-paste (Platisol T/SP) were purchased from Salaronix. FTO glass plates were cleaned in a detergent solution using an ultrasonic bath for 30 min and then rinsed with water and ethanol. Next, the plates were immersed into a 40 mM aqueous $TiCl_4$ at 70°C for 30 min in a chamber. After being washed with deionized water and fully rinsed with ethanol, a transparent nanocrystalline layer was prepared on the FTO glass plates by using a screen-printing technique. TiO_2 paste was dried for 5 min at 150°C. The TiO_2 electrodes were finally heated under an air atmosphere at 450°C for 30 min. The TiO_2 electrodes were treated again with $TiCl_4$ at 70°C for 30 min and sintered at 450°C for 30 min. A TiO_2 film comprising a 10-11 μm-thick transparent layer was obtained as checked using profilometer. The prepared TiO_2 film on the FTO electrode was immersed in 0.5 mM acetonitrile dye solution containing Chenodeoxycholic acid (0.1 mM) at room temperature overnight and finally quickly rinsed with acetonitrile before assembly. FTO plates for the counter electrodes were cleaned in an ultrasonic bath in acetone. The counter electrodes were prepared by screen-printing of Platisol onto the FTO coated glass substrate and then heated at 450°C for 30 min under air atmosphere. The platinum counter electrodes and the dye-adsorbed TiO_2 electrodes were assembled into a sealed sandwich-type cell by heating at 80°C using a hot-melt film (30 μm spacer Surlyn) between the electrodes. A drop of AN50 solution was placed in the drilled hole of the counter electrode. Finally, the hole was sealed using additional Surlyn and a cover glass (0.1 mm thickness). The photovoltaic characterization of the Fe-carbene-sensitized TiO_2 cells was obtained using two complementary techniques. The irradiated surface was 0.36 cm^2. The spectral response was determined by measuring the wavelength dependence of the incident photon-to current conversion efficiency (IPCE) using light from an Osram 300-W xenon lamp coupled to a Newport monochromator (Oriel Cornerstone 260). Photocurrents were measured under short circuit conditions (DC mode) using a Newport 1936R optical power meter. Incident irradiance was measured with a 1 cm^2 calibrated silicon photodiode. For J/V measurements we used the same lamp (Osram 300-W xenon) with an AM 1.5G filter solar spectrum in the 350-900 nm domain and a power of 100 mW / cm^2. Incident irradiance was measured with a ISO-Tech ISM410. The current–voltage characteristics were determined by applying an external potential bias to the cell using a Radiometer potentiostat (PGP 201) sweeping the potential with a scan rate of 10 m V/s.

2.3 Computations

The semiconductor surface was modeled by a neutral stoichiometric $(TiO_2)_{82}$ cluster of ca. 2x2 nm side, obtained by "cutting" an anatase slab exposing the majority (101) surface.[70, 71] This cluster model provides energy levels in close agreement with experimental band edges of anatase TiO_2,[62, 72] when global hybrid functionals and implicit solvation models are employed. Ground state equilibrium geometry of the dye@TiO_2 assemblies were optimized in the gas phase with the ADF program package,[73] using the Becke-Perdew exchange-correlation functional[74, 75] and a DZP (C, H, O, N)/ TZP (Fe, Ti) basis set. The interfacial electronic structure was determined by single point DFT calculations in acetonitrile solution (ε = 37.5) carried out on the optimized dye@TiO_2 complexes using the hybrid B3LYP functional, a 6-31G* basis set and a polarizable continuum model of solvation (C-PCM)[76, 77] as implemented in the Gaussian09 package.[78]

In a simple Newns-Anderson picture, the broadening of the dye's lowest unoccupied molecular orbital (LUMO) projected density of states (PDOS) over the semiconductor CB states can be used to calculate the injection time.[79-84] As recently shown,[85] however, this approach, based on the Mulliken population analysis for the determination of the PDOS, is significantly sensitive to the basis set quality. A more quantitative calculation of the coupling between the dye's donor states and the CB states can be obtained in a diabatic-like scheme, proposed by Thoss and co-workers[86, 87] and detailed in the following.

To estimate the efficiency of the electron/hole injection from the dye to the semiconductor, we resorted to a Fermi golden rule framework, where the injection rate k_{inj} (whose inverse is the injection time τ) is defined as:

$$k_{inj} = \frac{2\pi}{\hbar}\sum_{k} \left|V_{dk}\right|^2 \rho(\varepsilon_k) \qquad (1)$$

where the k represents the manifold of TiO_2 acceptor (conduction or valence band) states of interest and d is the dye donor state (LUMO in the case of injection and HOMO in the case of recombination). The product between the square of the electronic coupling elements, $|V_{dk}|^2$, and the semiconductor density of states (DOS), $\rho(\varepsilon_k)$, defines the electron transfer probability distribution $\Gamma(\varepsilon_k)$. The diabatic donor (dye) and acceptor (TiO_2) states were obtained by localization of the molecular orbitals of the entire complex on the donor and acceptor species. This results in a block Fock matrix of the interacting dye@TiO_2 system, where the diagonal elements represent the energies of the localized states, while the off-diagonal blocks contain the coupling elements V_{kd}. Finally injection times can be calculated as $t(\text{fs}) = \frac{658}{\Gamma(\text{meV})}$.

3. Results and Discussion

3.1 Photovoltaic characterization of homoleptic Fe(II)-NHC complexes

The photovoltaic properties of **C2** based DSSCs have been reported by some of us in Ref. [52], while for the **C4** complex, featuring benzimidazolydene(BIm)-based ligands and showing a record ^{3}MLCT lifetime efficiency of 26 *ps*, solely the synthesis and photophysical characterization have been published up to now.[54] Since **C4** presents a longer excited state lifetime, and thus a larger time window for carrier injection than **C2**, and comparable optical and structural properties, one might expect similar or even better photovoltaic performances in working DSSCs.

Figure 2 displays the UV-Vis absorption spectra of the complexes in acetonitrile (A) and sensitized TiO_2 film (B) as well as the IPCE (C) and J/V (D) curves for the cells fabricated with **C2** and **C4**, while the photovoltaic and surface loading data are listed in Table 1. In acetonitrile solution, **C2** presents an absorption peak, associated to the singlet MLCT states, at 520 nm (2.38 eV) with and extinction absorption coefficient of 16200 $M^{-1}cm^{-1}$, while the lowest-energy absorption band of **C4** appears slightly blue-shifted (501 nm/2.48 eV) and with an absorbance lower by about 20% (12800 $M^{-1}cm^{-1}$, Table S1 in Supporting Information). Regarding the optical UV-Vis absorption spectra of the sensitized anatase films (Figure 2B), the **C4**@TiO_2 absorbance appears to be almost half of that recorded for **C2**@TiO_2, clearly suggesting a less efficient surface coverage. The estimated dye loads are indeed 0.09 and 0.06 μmol cm^{-2} for **C2** and **C4**, respectively, to be compared with the value of 0.08 μmol cm^{-2} recorded in the same conditions for **N719**. Since there are in principle no reasons to hypothesize a different adsorption mode for **C4** with respect to **C2**, the lower coverage seems to be ascribable to the presence of the bulky BIm substituents, which almost double the dye volume.

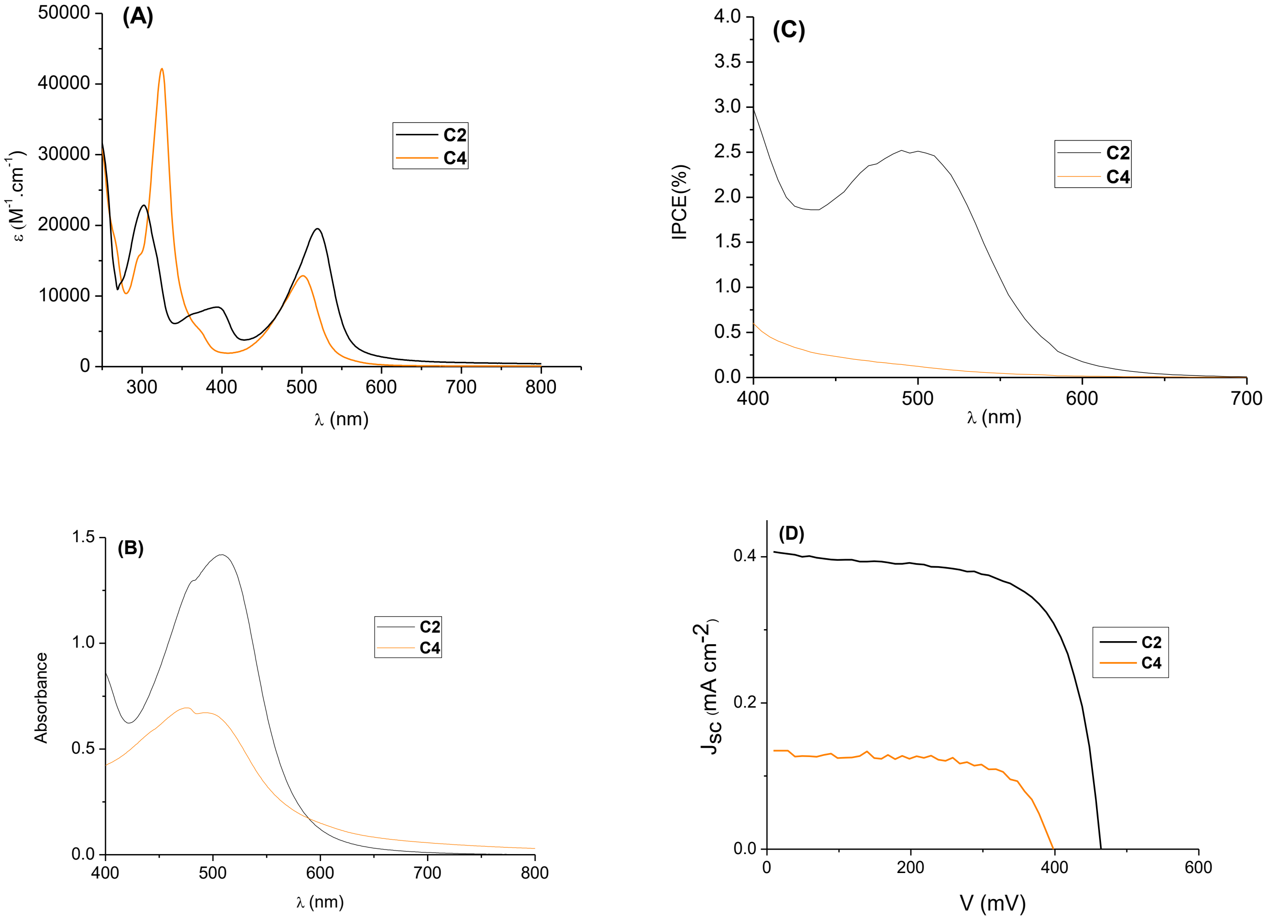

Figure 2. UV-Vis absorption in acetonitrile (A). UV-Vis absorption spectra of the sensitized TiO_2 film (B), IPCE (C) and J/V (D) curves for DSSCs based on **C2** and **C4.**

Table 1. Photovoltaic performances of DSSCs fabricated with the **C2** and **C4** dyes and the reference N719 dye.[a]

Dye	**J_{SC}** (*$mA.cm^{-2}$*)	**V_{OC}** (*mV*)	**FF**	**η%**	**Dye load** (*$\mu mol\ cm^{-2}$*)[b]
C2	0.41	457	0.68	0.13	0.09
C4	0.12	368	0.71	0.03	0.06
N719	13.25	687	0.67	6.1	0.08

[a] Measurements performed under AM 1.5 G irradiation (100 mW.cm^{-2}), irradiated area: 0.36 cm^2 on TiO_2 layers (10–11 μm). Values obtained from at least three DSSCs per dye. [b] Dye load calculated from absorbance data of the sensitized electrode. Values confirmed by desorption of dyes from TiO_2 under basic conditions.

IPCE plots (Figure 2C) recorded for devices employing the I_3^-/I^- redox couple and CDCA, to suppress dye aggregation, show that while an appreciable, even if modest, IPCE was recorded (about 2.3% at 500 nm) for **C2**, for the cell fabricated with **C4** basically only negligible electron injection into the semiconductor was detected (about 0.2% at 500 nm). The measured photocurrent density for the **C4-**sensitized solar cell is more than three times lower than that measured for **C2** (0.12 vs. 0.41 mA cm^{-2}) and a 20% reduction in V_{oc} is also observed. Both the poor performance of the **C4** complex, and the extremely low photocurrents measured for **C2**, despite its good optical and photophysical properties and the reported 92% injection yield,[49] seem to indicate an inefficient interfacial charge separation process, possibly associated to fast recombination reactions, observed to take place in the picosecond and nanosecond time scale.[49] Importantly, as shown in Table 1, the surface dye load value for **C2** is even larger then that of the N719 reference dye, allowing us to leave out any problem related to an inefficient TiO_2 sensitization.

3.2 Structural and electronic properties of the Fe(II)-NHC interfaces

To shed light on the efficiency of the interfacial hole and electron transfer processes, here we shall characterize, by means of DFT calculations, the structural and charge separation properties of the sensitized-TiO_2 interfaces.

The ground state optimized structures of the **C2** and **C4** complexes adsorbed on the $(TiO_2)_{82}$ cluster are shown in Figure S1 in Supporting Information. Here we consider the bidendate anchoring of the carboxylate to the undercoordinated Ti atoms of the (101) anatase surface, which is well-known to be the energetically favored one.[61] A first comment concerns the geometrical arrangement of the molecules on the surface. In both cases the complexes appear to be markedly tilted on the semiconductor surface, forming an angle of approximately 45 degrees with the TiO_2 plane. This is consistent with the coordination geometry recently reported for the analogous heteroleptic complex of C2 on an anatase-$(TiO_2)_{92}$ slab.[51] The strong tilt towards the surface also yields a slight elongation of the O—Ti distance, which increases from the typical 2.05-2.10 Å value, calculated for adsorbed carboxylate groups, to an average value of 2.20-2.25 Å.

The electronic structure and energy level alignment of the dye-sensitized TiO_2 interface can be analyzed by inspection of the Projected Density of States (PDOS) and frontier molecular orbitals (MOs), as depicted in Figure 3 for **C2** (top) and **C4** (bottom), where the % contribution of localization on the dye of the relevant frontier MOs is also indicated. From the energetic point of view, the Fe(II)-carbene/TiO_2 interfaces resemble the typical alignment of Ru(II)-polypyridyl/TiO_2 interfaces, with the highest occupied MOs lying above the semiconductor valence band (VB) and the lowest unoccupied MO above the semiconductor CB edge, that here we calculate at -3.46/-3.47 eV for **C2**@TiO_2/**C4**@TiO_2. As is apparent, both **C2** and **C4** have HOMOs delocalized over the whole molecular skeleton and presenting a sizeable mixing with the TiO_2 VB states (around 30-50%), manifested by the tail of the TiO_2 VB PDOS extending through the dye's HOMOs PDOS. Going from **C2** to **C4** the calculated dye's HOMO shifts from -5.70 to -5.96 eV, with a stabilization of 0.26 eV, that, within the simplest Koopman's approximation, almost quantitatively compares with that experimentally measured shift (0.28 eV) in the Fe^{III}/Fe^{II} oxidation potentials (Table S1 in Supporting Information).

However, a deeper analysis of the topology and alignment of the unoccupied states may deliver us more precise information on the interfacial charge separation and electron injection capability.

For both **C2**/**C4** we find that the dye's LUMO, calculated at -2.63/-2.71 eV, respectively, is essentially not coupled with the semiconductor CB states: it is, in fact, almost completely localized on the dye (93% and 97% for **C2** and **C4** respectively) and, above all, it extends over the ligand not anchored to the TiO_2 surface (see isodensity plots in Figure 3). On the other hand, the LUMO+1 distribution is markedly broadened and strongly coupled with the CB states (see the appreciable electronic density on the TiO_2 slab appearing in the isodensity plots in Figure 3). A 100% dye's LUMO+1 population is, in fact, obtained summing over 190 and 150 dye-TiO_2 mixed states in the case of **C2** and **C4**, respectively. As is apparent from the plots of the isodensity surfaces in Figure 3, in the lower energy tail is dominated by contributions mainly localized on the anchoring moiety with strong delocalization toward the CB TiO_2 states, while at higher energies still large density contributions on the not anchored ligand appear, above all for **C2**. Thus, even if the interfacial energetics would allow electron injection, as discussed in Ref.[49], the primary charge transfer character for the lowest MLCT state appears to be in the opposite direction to the one necessary to inject into the TiO_2 CB. This fact is the direct result of the adsorption of the dye onto the TiO_2 surface: the near-degeneracy between the two lowest unoccupied orbitals localized on the two ligands[52] in the isolated complexes is removed upon COOH deprotonation and subsequent binding to the Ti atoms. As the TiO_2 is a weaker electron acceptor than the opposite H^+, the orbital localized on the anchored ligand turns out to be destabilized with respect to the one bearing the free COOH group. A structural distortion in the anchored dye can also contribute in the relative stabilization/destabilization of the LUMO and LUMO+1. In particular, since the LUMO (LUMO+1) is considerably delocalized on the COOH unit one can expect a sizeable destabilization upon deprotonation and, indeed, considering the isolated **C2** complex in acetonitrile solution, we calculated (B3LYP/6-31G*) an upshift of about 0.8 eV of the Kohn-Sham eigenvalue of the associated unoccupied MO. Coordination to the anatase surface clearly reduces this energy penalty, even if a LUMO-LUMO+1 energy difference of about 0.4 eV still remains.

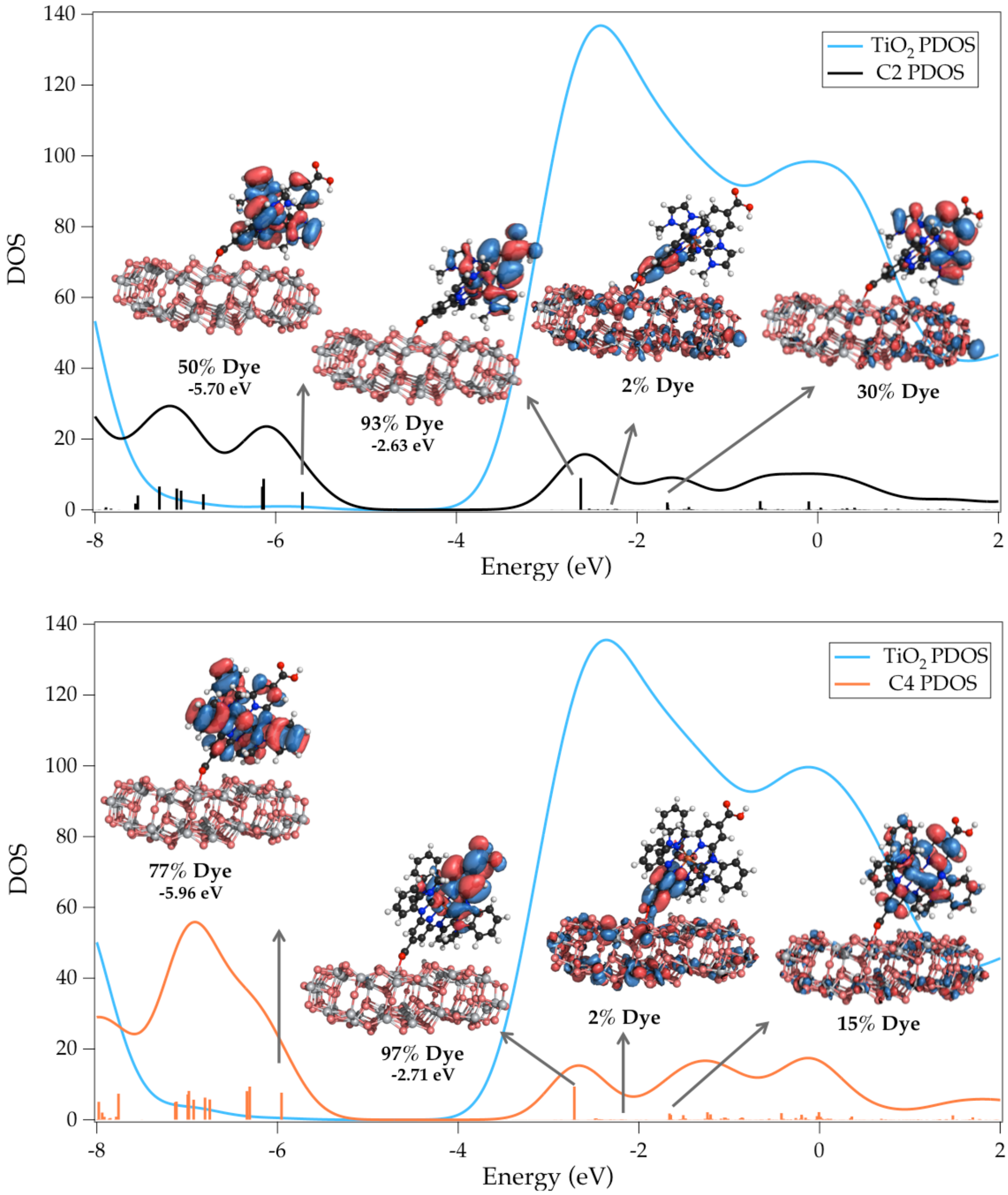

Figure 3. Projected DOS (PDOS) and main dye's MOs isodensity plots for the **C2** (top) and **C4** (bottom) complexes adsorbed onto the $(TiO_2)_{82}$ cluster. For the depicted MOs the % contribution of population localized on the dye is also indicated. The gaussian broadening used to reproduce the PDOS is equal to 0.3 eV. Vertical sticks represent the Khon-Sham eigenvalues and their intensity the % dye's population.

With this information in mind, it is interesting to do a step backward and notice the marked broadening and weak, but still appreciable, splitting in the absorption spectra maxima of the **C2**- and **C4**-sensitized TiO_2 films (Figure 2 B). It is worthwhile to stress, however, that the extent of the energy separation between these two MLCT states crucially depends on the cell preparation and working conditions. The use of ionic additives in the electrolyte, acidic treatment of the TiO_2 substrate, pH conditions and coexistence of multiple anchoring modes can interplay in restoring/removing their near degeneracy. In fact, as shown by the PDOS in Figure 4, the deprotonation of the not-coordinated COOH group in **C2** is sufficient to invert the LUMO/LUMO+1 nature and to redirect the charge flow of the lowest energy MLCT state toward the surface, guarantying a strong coupling with the TiO_2 CB states. In line with what discussed above for the LUMO+1 population, we notice that the LUMO distribution also contains significant contributions on the not-anchored ligand (a MO with about 67% of population on the dye is found at -1.78 eV). Another beneficial effect of deprotonation seems to be the change in the nature of the highest occupied MO. The HOMO is in fact upshifted at -5.19 eV and it turns out to be strictly localized far from the surface, with no coupling (99% on the dye) with the TiO_2 states and thus less prone to give recombination with injected electrons. However, operating in a strong basic environment in order to maintain the not-coordinated carboxylic group in its deprotonated form and thus inverting the direction of the lowest excited state charge flow, is not possible in practice without desorbing the grafted dyes from the substrate. Thus, omitting one of the carboxylic groups and moving to heteroleptic complexes appears the only feasible way to prevent the deactivation pathway by promoting a unidirectional electron channel toward the semiconductor CB. We report in the bottom panel of Figure 4 the calculated PDOS and plots of the frontier MOs for the heteroleptic analogous of **C2** (termed **C5** in Figure 1). The results confirm the desired charge transfer nature of the lowest energy dye level and overall agree with the electronic structure reported in Ref.[51] for the same complex adsorbed on a $(TiO_2)_{92}$ slab and calculated at PBE0 level of theory.

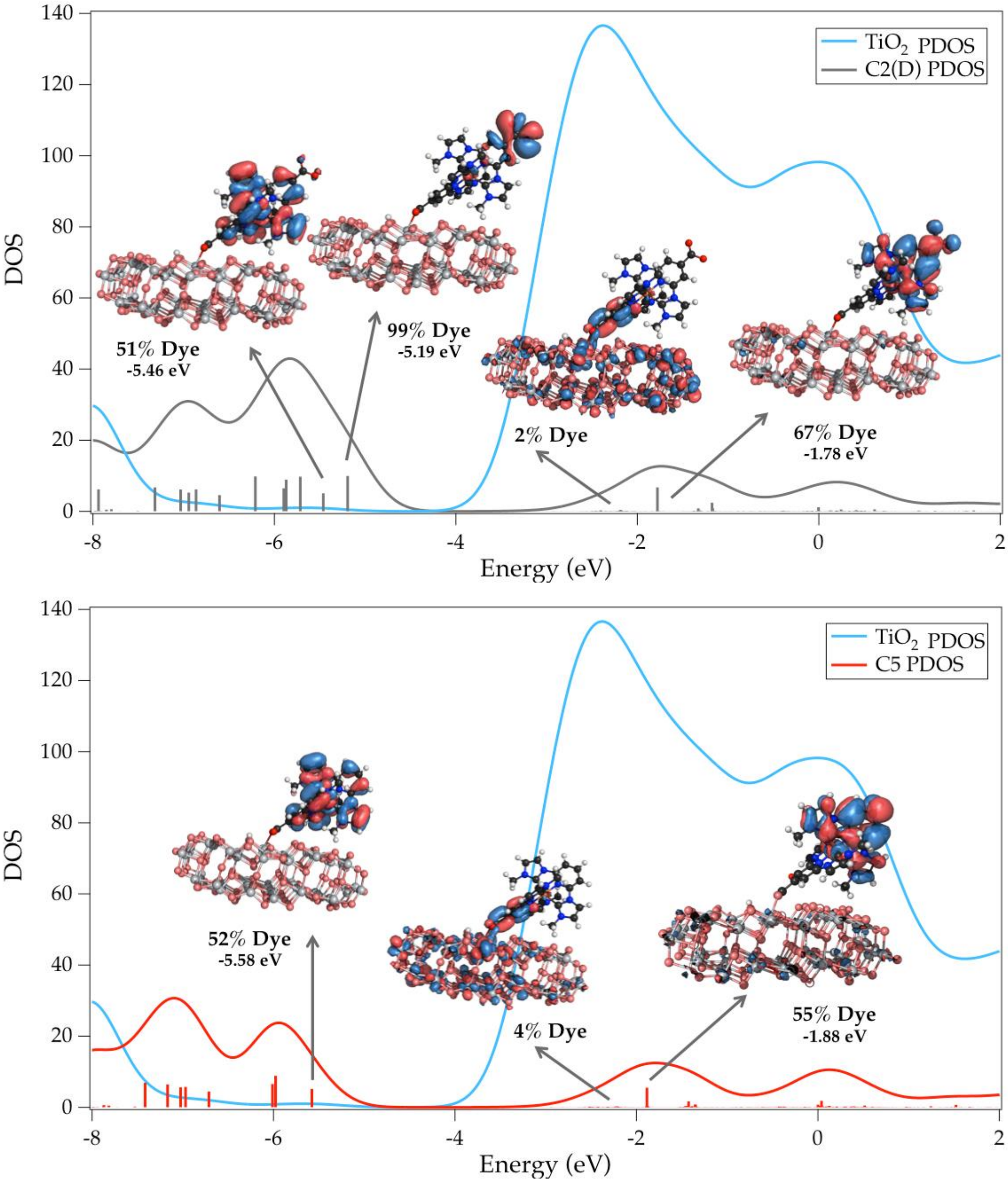

Figure 4. Projected DOS (PDOS) and main dye's MOs isodensity plots for the deprotonated **C2(D)** (top) and heteroleptic **C5** (bottom) complexes adsorbed onto the $(TiO_2)_{82}$ cluster. For the depicted MOs the % contribution of population localized on the dye is also indicated. The gaussian broadening used to reproduce the PDOS is equal to 0.3 eV. Vertical sticks represent the Khon-Sham eigenvalues and their intensity the % dye's population.

3.4 Photovoltaic characterization of heteroleptic Fe(II)-NHC complexes

On the basis of the electronic structure of the **C5**@TiO_2 complex discussed above, heteroleptic compounds should be able to effectively inject electrons into the semiconductor CB. We therefore prepared the three heteroleptic Fe(II)-carbene complexes **C5**, **C6** and **C7** (see Figure 1 and Supporting Information for preparation) and investigated their electronic and photovoltaic properties (Figure 5 and Table 2). Besides **C5**, the heteroleptic analogous of **C2**, we also investigated the effect of electron-donating substituents such as anisyl and triphenyl amine on the NHC ligands **C6** and **C7** with the idea of i) increasing the polarization of the dye and thus enhancing the electron transfer; ii) maintaining the photo-generated hole far from the semiconductor surface to possibly limit the injected electrons recapture.

The recorded UV-Vis spectra in acetonitrile (A), on the TiO_2 film (B), the IPCE (C) and J/V (D) curves for all the heteroleptic complexes along with those of the reference **C2** homoleptic complex are reported in Figure 5, whereas Table 2 compiles the associated photovoltaic data. The UV-Vis absorption maxima in solution and on TiO_2 as well as the redox properties of the complexes are collected in Table S1 in Supporting Information.

The absorption spectra of the complexes in acetonitrile (Figure 5A) clearly show the effect of the dissymmetric structure of the heteroleptic complexes. Indeed, while the homoleptic complex **C2** exhibits two MLCT transitions in the visible domain at 394 nm (metal-carbene MLCT) and 520 nm (metal-pyridine MLCT), an additional MLCT band was observed for the heteroleptics at 430 nm.

In the visible region, complexes **C5**, **C6** and **C7** have a similar three-band spectrum with variations in the ε values, the anisyl substituent in complex **C6** promoting a significant increase of the absorption. In the UV region compound **C7** featured the characteristic intense band (296 nm, ε=40600 $M^{-1}.cm^{-1}$) of the π–π* transition on the triphenylamine moiety.

The removal of one carboxylic acid going from **C2** to the heteroleptic complexes induced a significant blue shift of the lowest energy transition band from 520 nm to ca. 509 nm, while the band at 394 nm corresponding to the metal-carbene transition[52,54] remained unchanged. Thus the band at 430 nm in heteroleptic complexes can be attributed to the MLCT transition between the iron center and the ligand with the unsubstituted pyridine. Interestingly, the band at 509 nm appears much more intense than the others for every complex indicating that a higher amount of light energy was absorbed by the MLCT transition involving iron and the carboxypyridine. This augmented absorbance should in principle translate into higher IPCE values in DSSCs.

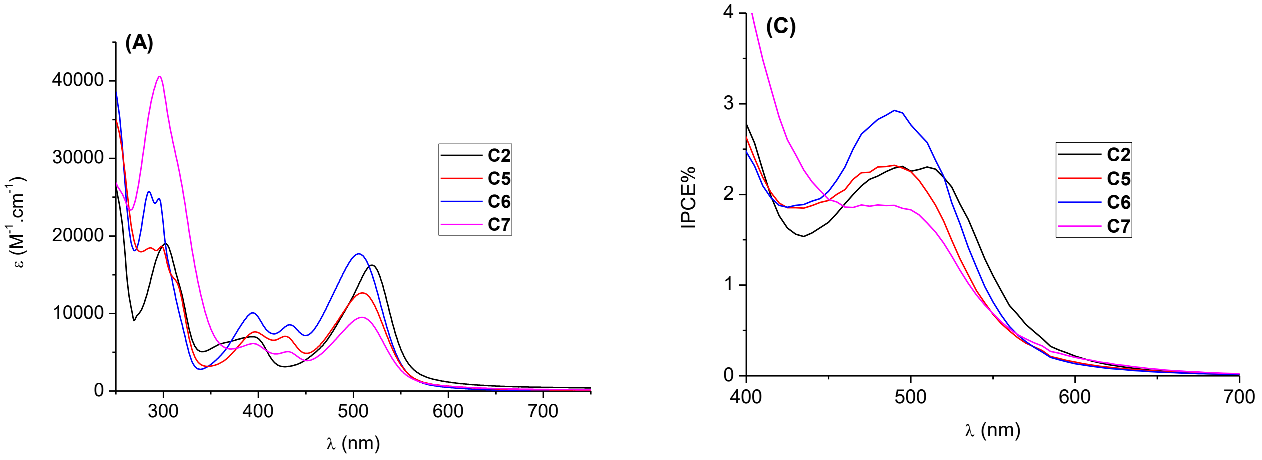

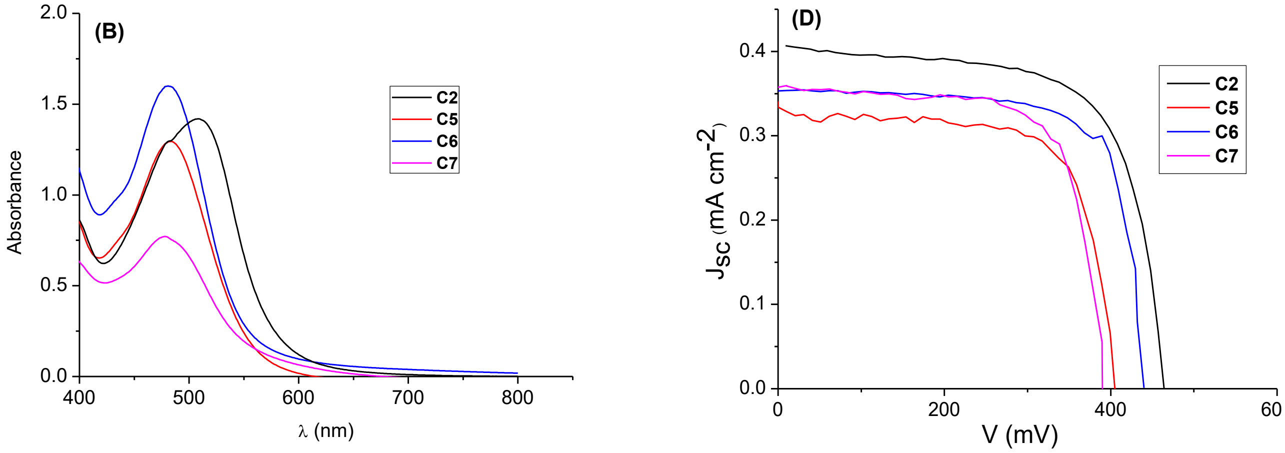

Figure 5. UV-Vis absorption in acetonitrile (A). UV-Vis absorption spectra of the sensitized TiO_2 film (B), IPCE (C) and J/V (D) curves for DSSCs based on **C2, C5**, **C6** and **C7.**

The absorption spectra of the sensitized electrodes (Figure 5B) perfectly mimicked the solution spectra with the blue-shift of the MLCT band in heteroleptics compared with **C2** and the best absorbance measured for complex **C6**. IPCE curves (Figure 5C) showed that the dyes were able to harvest light and produce carriers along a wide absorption window. As a consequence of its better absorbance, complex **C6** permitted to reach a 3 % IPCE vs 2.5% for **C5** and the homoleptic **C2**.

As is apparent, however, from the J/V curves (Figure 5D) and PV data in Table 2, despite possessing the desired interfacial charge separation characteristics the photovoltaic performances of the cells fabricated with all the heteroleptic derivatives did not show any improvement compared to the efficiency obtained with the homoleptic **C2** complex (Table 1). The overall efficiencies of the cells fabricated with the heteroleptic complexes are around 0.1%, with photocurrent values of 0.33 (**C5**) and 0.36 (**C6** and **C7**) $mA\ cm^{-2}$. Comparable and even larger surface coverage values are also obtained, with the only exception of **C7**, bearing the bulkier triphenylamine substituents, thus comparable light harvesting capabilities for the sensitized-TiO_2 films can be hypothesized. As a matter of fact, very low V_{oc} values were also obtained, being in all cases around 400 mV, whereas the V_{oc} measured for the N719 Ru(II) complex in the same operating conditions is around 690 mV (Table 2). These extremely low photovoltage and photocurrent values clearly suggest an unfavorable balance between the interfacial electron injection and recombination (with both oxidized dye and electrolyte)[88] pathways. Concerning the recombination with the electrolyte, it is interesting to notice that such low V_{oc} values resemble those reported in the literature for phtalocyanine[89] and other purely organic and metal centred dyes[90] in combination with the I^-/I_3^- redox couple.[91] These results are usually attributed to the possible formation of stable complexes[92] between the aromatic ligands and/or particular functional groups and the electrolyte species. The formation of these adducts yields to an increased concentration of iodine in proximity of the TiO_2 surface, boosting the recombination probability. We also notice that the highly delocalized nature of the HOMO (hole in the oxidized dye), appearing in Figures 3 and 4, and the markedly bent adsorption configuration (Figure S1 in Supporting Information) of these Fe(II)-NHC complexes might further favor the approach of the electrolyte to the semiconductor surface in the regeneration process.

Table 2. Photovoltaic performances of DSSCs fabricated with the heteroleptic **C5, C6** and **C7** dyes compared to the reference homoleptic **C2** and **N719** dyes.[a]

Dye	**J_{SC}** (*$mA.cm^{-2}$*)	**V_{OC}** (*mV*)	**FF**	**η%**	**Dye load** (*$\mu mol\ cm^{-2}$*)[b]
C5	0.33	400	0.73	0.10	0.10
C6	0.36	440	0.73	0.11	0.12
C7	0.36	390	0.71	0.10	0.07
C2	0.41	457	0.68	0.13	0.09
N719	13.25	687	0.67	6.1	0.08

[a] Measurements performed under AM 1.5 G irradiation (100 $mW.cm^{-2}$), irradiated area: 0.36 cm^2 on TiO_2 layers (10–11 μm). Values obtained from at least three DSSCs per dye. [b] Dye load calculated from absorbance data of the sensitized electrode. Values confirmed by desorption of dyes from TiO_2 under basic conditions.

3.4 Interfacial electron injection and recombination

On the basis of electronic structure calculations of the Fe(II)-NHC@TiO_2 complexes discussed above and upon localization of the MOs on the dye and TiO_2 fragments, we can quantitatively estimate the rates for both the electron injection from the dye's LUMO (or LUMO+1) into the CB states and hole injection from the dye's HOMO to the CB states (i.e. recombination to the oxidized dye). The results are depicted in Figure 6 in terms of probability distribution Γ*(k)* and diabatic Density of acceptor TiO_2 states (see eq. 1) along with the relevant dye energy levels, while Table 3 summarizes the calculated injection probabilities extracted at the energy of the donor states (LUMO/LUMO+1 and HOMO for electron injection and recombination, respectively). Since **C5**, **C6** and **C7** exhibited similar electronic properties we focused on **C5** for a better comparison with its homoleptic counterpart **C2**. The energies of the corresponding diabatic levels, shown by vertical sticks in Figure 6, are given in Supporting Information (Table S2).

Table 3. Probability distributions, Γ(eV), DOS (number of states/eV) calculated at the diabatic HOMO, LUMO and LUMO+1 energies, and associated injection rates, k_{inj} (s^{-1}).

<table>
<tr><td colspan="7"><i>Electron injection</i></td></tr>
<tr><td>System</td><td>Γ (ε_{LUMO})</td><td>DOS (ε_{LUMO})</td><td>k_{inj}</td><td>Γ (ε_{LUMO+1})</td><td>DOS (ε_{LUMO+1})</td><td>k_{inj}</td></tr>
<tr><td>C2@TiO_2</td><td>2.03×10^{-4}</td><td>129</td><td>1.9×10^{12}</td><td>0.158</td><td>133</td><td>1.5×10^{15}</td></tr>
<tr><td>C4@TiO_2</td><td>1.67×10^{-4}</td><td>120</td><td>1.6×10^{12}</td><td>0.120</td><td>136</td><td>1.1×10^{15}</td></tr>
<tr><td>C2(D)@TiO_2</td><td>0.162</td><td>129</td><td>1.5×10^{15}</td><td>1.1×10^{-3}</td><td>114</td><td>1.0×10^{13}</td></tr>
<tr><td>C5@TiO_2</td><td>0.010</td><td>130</td><td>9.5×10^{13}</td><td>1.2×10^{-3}</td><td>120</td><td>1.1×10^{13}</td></tr>
<tr><td colspan="7"><i>Recombination to the oxidized dye</i></td></tr>
<tr><td></td><td colspan="2">Γ (ε_{HOMO})</td><td colspan="2">DOS (ε_{HOMO})</td><td colspan="2">k_{inj}</td></tr>
<tr><td>C2@TiO_2</td><td colspan="2">1.0×10^{-11}</td><td colspan="2">1×10^{-8}</td><td colspan="2">9.5×10^{4}</td></tr>
<tr><td>C4@TiO_2</td><td colspan="2">5.0×10^{-10}</td><td colspan="2">3×10^{-6}</td><td colspan="2">4.8×10^{7}</td></tr>
<tr><td>C2(D)@TiO_2</td><td colspan="2">1.8×10^{-15}</td><td colspan="2">6×10^{-8}</td><td colspan="2">17</td></tr>
</table>

C5@TiO$_2$	3.0 x 10^{-12}	6 x 10^{-9}	2.6 x 10^4

A first comment concerns the homoleptic complexes (**C2** and **C4**). In agreement with the electronic structure reported in Figure 3 and discussed above, the plots in the top panel of Figure 6 and the related data in Table 3 show that the electronic coupling between the dye's LUMO and the semiconductor CB states is negligible. The calculated Γ values extracted at the energy of the dye's donor state (LUMO) are of the order of 10^{-4} eV, resulting in calculated injection rates of about 10^{12} s^{-1}. In other words, the electron injection is predicted to take place in the *ps* timescale, which is exactly the timescale for the deactivation of the ^{3}MLCT state (16 ps and 26 ps, for **C2**[52] and **C4,**[54] respectively). Notably our calculations are also able to provide a quantitative difference between **C2** and **C4**, predicting for the latter a lower injection probability (Γ), over the whole manifold of CB states, possibly due to the higher delocalized character of the MOs induced by the presence BIm substituents. As expected, on the other hand, the typical ultrafast injection mechanism characteristic of the Ru(II)-polypyridyl complexes is envisaged for LUMO+1, with Γ values of the order of 10^{-1} eV and injection rates of 10^{15} s^{-1} (*fs* timescale). Also in this case, for **C4** a slower injection rate is calculated at the LUMO+1 energy level and the Γ curve is always lower than that calculated for **C2** (see Figure S2 in Supporting Information). As deprotonation of the not-coordinated COOH group inverts the energetic order between the LUMO and LUMO+1 levels, restoring the desired interfacial charge separation, $\Gamma(\varepsilon_{LUMO})$ for **C2(D)** is of the same order of magnitude of $\Gamma(\varepsilon_{LUMO+1})$ calculated for the protonated **C2** (0.162 vs. 0.158 eV) and an injection rate in the *fs* timescale is predicted. It is worthwhile to notice in the middle panel of Figure 6, that almost coincident Γ curves are obtained for the LUMO+1 of **C2** (black) and LUMO of **C2(D)** (grey), confirming the identical nature of the diabatic states in the two systems. On the other hand, the injection probability distributions of the heteroleptic **C5** complex (red curve in the middle panel of Figure 6) indicates an appreciable change in the electronic structure, i.e. in the diabatic LUMO nature, delivering lower electronic coupling with the low-energy TiO$_2$ CB states (where the LUMO is energetically located) and larger coupling with higher-energy states (around -1.5 eV). The electronic coupling elements calculated for the LUMO/LUMO+1 of **C5**/**C2** and the TiO_2 CB states are reported in Figure S3 in Supporting Information. Thus the calculated $\Gamma(\varepsilon_{LUMO})$ for **C5** is more than one order of magnitude lower than that calculated for the deprotonated complex (0.010 vs. 0.162 eV), resulting in a longer injection time, lying in the range of several *ps* in the same time scale of the ^{3}MLCT lifetimes of the heteroleptic complexes, measured at 14, 10 and 12 ps for **C5**, **C6** and **C7** respectively (see Figure S6 and Table S3 in Supporting Information)

Interesting insights also comes from the hole injection Γ curves describing the recombination processes from the dye's HOMO to the TiO_2 CB states (bottom panel of Figure 6). In line with the typical measured *ms* time scales for Ru(II)-polypyridyle sensitizers, in our diabatic-like framework recombination to the oxidized dye is calculated to be extremely slow, as a consequence of the negligible energetic overlap between the dye HOMO and the TiO_2 CB states. We however note that for **C2**, **C5** and **C4 (**even if at a lower extent) the Γ plots (black, red and orange lines, respectively) and V values (eq. 1) plotted in Figures S4 and S5 in Supporting information, indicate a sizeable electronic coupling with both the VB and CB states due to the above discussed high delocalization of the HOMO favoring electronic conjugation with the TiO_2 MOs. This inefficient interfacial hole/charge separation suggests that in the complexity of the dye-sensitized TiO_2 interface, where heterogeneous binding modes and supramolecular interactions alter the energetic alignment calculated here, the actual recombination rate to the oxidized dye might be higher, occurring in the nanosecond and even picosecond timescale, as reported in Ref. [49] The hole injection (recombination) rate of **C4** is however predicted to be three orders of magnitude faster than of those of **C2** and **C5** (10^7 s^{-1} to be compared to 10^4 s^{-1}), as a consequence of the higher TiO_2 DOS (see the number of states listed in Table 3). Then, as expected, the coupling for the HOMO of the deprotonated **C2(D)** is, instead, almost zero (see the solid grey curve in the bottom panel of Figure 6), with a practically suppressed recombination rate, predicted to occur in the second timescale.

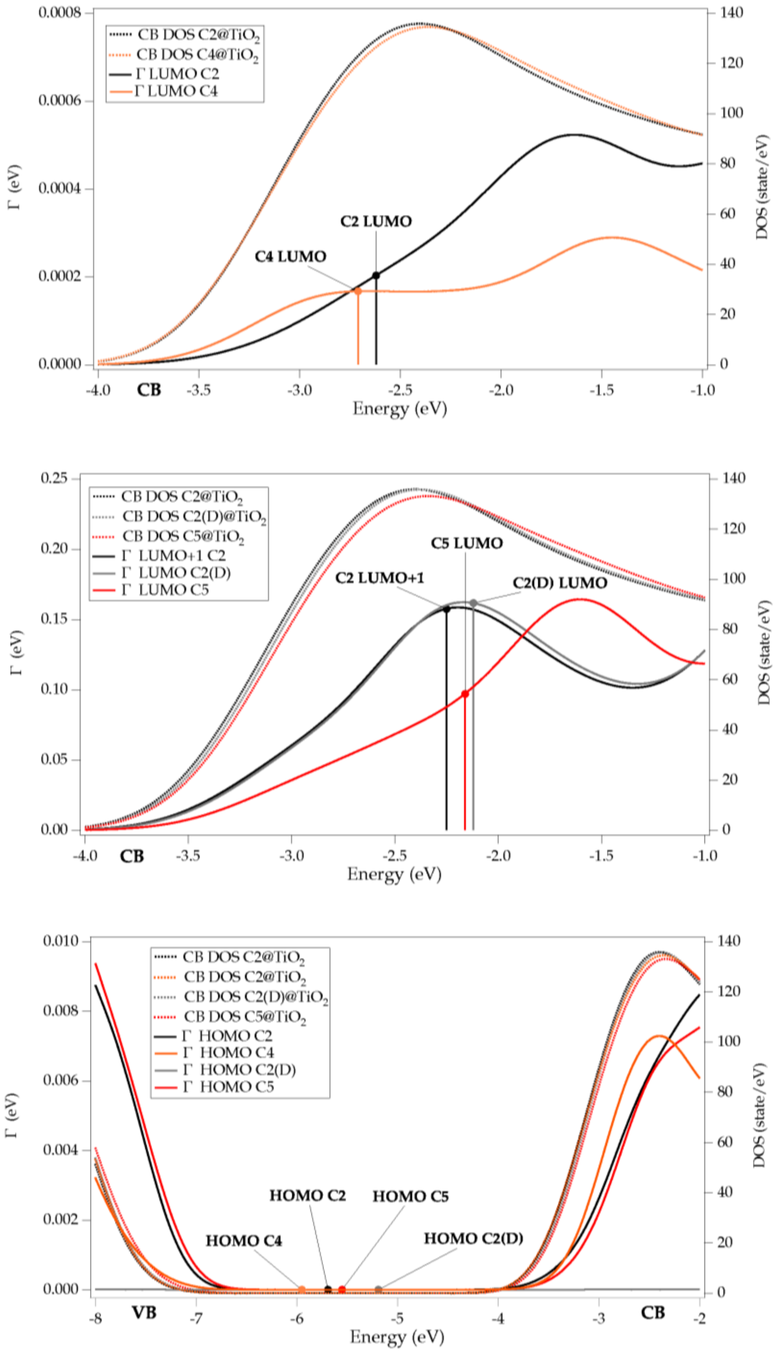

Figure 6. Probability distribution Γ(ε_k), left scale, solid line, (eV); and diabatic Density of States (DOS, right scale, dashed lines eV^{-1}) for electron injection from the C2/C4 LUMO (top), C2 LUMO+1 and C2(D)/C5 LUMO (middle) to the TiO$_2$ CB, and hole injection from the C2/C2(D)/C4/C5 HOMO to the TiO$_2$ VB (bottom). The relevant dye energy levels are also reported as vertical sticks.

4. Summary and Conclusions

Here we have reported for the first time a combined theoretical and experimental (photovoltaic) characterization of Fe(II)-carbene sensitized photoelectrodes in working solar cells. In addition to the already developed homoleptic Fe(II)-NHC **C2**[52] and **C4**[54] complexes (Figure 1), the synthesis, characterization and photovoltaic application of three new heteroleptic Fe(II)-NHC dye sensitizers (**C5**, **C6** and **C7**, Figure 1) has been carried out. Despite an improved interfacial charge separation, the heteroleptic compounds did not show boosted photovoltaic performances compared to the homoleptic ones: photocurrent values of about 0.3-0.4 *mA* cm^{-2}, V_{oc} of ca. 400 mV and overall efficiency of 0.1% are obtained for all the investigated sensitizers. The quantitative analysis of the interfacial electron and hole transfers extracted from our quantum mechanical calculations, along with the measured photovoltaic data, clearly evidence the main problems associated to the poor device efficiencies and the main challenges that have to be faced to develop efficient iron-based sensitizers: i) fast recombination reactions with both oxidized dye and I^-/I_3^- electrolyte appears as the main barrier to efficient Fe(II)-NHC dyes; ii) homoleptic complexes do not present the desired directional electron flow toward the TiO_2 surface in their lowest MLCT state; iii) heteroleptic complex, although possessing the proper interfacial charge separation, are predicted to have lower electron injection rates when compared to the reference Ru(II)-polypyridyl complexes, yielding improved photocurrent and photovoltage values in working devices. Importantly, the calculations revealed that the deprotonation of the not anchored carboxylic function in the homoleptic **C2** complex (**C2(D)**) promoted a notable speeding up of the electron injection (from the *ps* for **C2** to the *fs* time scale for **C2**(**D**)) while suppressing the electron recombination. In this case, the interfacial hole/electron charge separation nicely resembles that of the reference N719 Ru(II) sensitizer. This result clearly indicates that the introduction of electron-donating substituents (as it is the case for the carboxylate function) on the not-anchored NHC ligand of heteroleptic complexes should be the route of choice to improve the overall interfacial charge generation and make iron-based dyes applicable for photoelectrochemical devices. Work is now in progress towards this direction.

Acknowledgments

Support from Université de Lorraine and CNRS is gratefully acknowledged. MP also thanks the contribution of the "Perspect H_2O" COST action CM1202. The authors thank S. Parant for setting up the photovoltaic measurements and F. Lachaud for ESI mass spectrometry.

References

1. Grätzel, M., *Acc. Chem. Res.* **2009,** *42*, 1788–1798.
2. Young, K. J.; Martini, L. A.; Milot, R. L.; Snoeberger Iii, R. C.; Batista, V. S.; Schmuttenmaer, C. A.; Crabtree, R. H.; Brudvig, G. W., *Coord. Chem. Rev* **2012,** *256*, 2503-2520.
3. Hamann, T. W., *Nat Mater* **2014,** *13*, 3-4.
4. Concepcion, J. J.; House, R. L.; Papanikolas, J. M.; Meyer, T. J., *Proc. Natl. Acad. Sci. USA* **2012,** *109*, 15560-15564.
5. O'Regan, B.; Grätzel, M.; Fitzmaurice, D., *J. Phys Chem.* **1991,** *95*, 10525-10528.
6. Hagfeldt, A.; Boschloo, G.; Sun, L.; Kloo, L.; Pettersson, H., *Chem. Rev.* **2010,** *110*, 6595-6663.
7. Snaith, H. J.; Schmidt-Mende, L., *Advanced Materials* **2007,** *19*, 3187-3200.
8. Jung, H. S.; Lee, J.-K., *J. Phys . Chem. Lett.* **2013,** *4*, 1682-1693.
9. Hardin, B. E.; Snaith, H. J.; McGehee, M. D., *Nat. Photonics* **2012,** *6*, 162.
10. Nazeeruddin, M. K.; De Angelis, F.; Fantacci, S.; Selloni, A.; Viscardi, G.; Liska, P.; Ito, S.; Takeru, B.; Grätzel, M., *J. Am. Chem Soc.* **2005,** *127*, 16835-16847.
11. Hagfeldt, A.; Peter, L., *Dye-sensitized Solar Cells* EPFL Press: Lausanne, 2010; p 323-403.
12. Han, L.; Islam, A.; Chen, H.; Malapaka, C.; Chiranjeevi, B.; Zhang, S.; Yang, X.; Yanagida, M., *Energy Environ. Sci.* **2012,** *5*, 6057-6060.
13. Pastore, M.; De Angelis, F.; Angeli, C., *Theor. Chem. Acc.* **2016,** *135*, 1-11.
14. Fantacci, S.; De Angelis, F.; Selloni, A., *J. Am. Chem Soc.* **2003,** *125*, 4381-4387.
15. Ardo, S.; Meyer, G. J., *Chem. Soc. Rev.* **2009,** *38*, 115-164.
16. Ashford, D. L.; Gish, M. K.; Vannucci, A. K.; Brennaman, M. K.; Templeton, J. L.; Papanikolas, J. M.; Meyer, T. J., *Chem. Rev.* **2015,** *115*, 13006-13049.
17. Listorti, A.; Creager, C.; Sommeling, P.; Kroon, J.; Palomares, E.; Fornelli, A.; Breen, B.; Barnes, P. R. F.; Durrant, J. R.; Law, C.; O'Regan, B., *Energy Environ. Sci.* **2011,** *4*, 3494-3501.
18. Listorti, A.; O,ÄôRegan, B.; Durrant, J. R., *Chem. Mater.* **2011,** *23*, 3381-3399.
19. Anderson, N. A.; Lian, T., *Annu. Rev. Phys. Chem.* **2004,** *56*, 491-519.
20. Lobello, M. G.; Fantacci, S.; De Angelis, F., *J . Phys. Chem. C* **2011,** *115*, 18863-18872.
21. Koops, S. E.; Barnes, P. R. F.; O'Regan, B. C.; Durrant, J. R., *J. Phys. Chem. C* **2010,** *114*, 8054-8061.
22. Yao, Z.; Zhang, M.; Wu, H.; Yang, L.; Li, R.; Wang, P., *J. Am. Chem. Soc.* **2015,** *137*, 3799-3802.
23. Kakiage, K.; Aoyama, Y.; Yano, T.; Oya, K.; Fujisawa, J.-i.; Hanaya, M., *Chem. Commun.* **2015**.
24. Ferrere, S.; Gregg, B. A., *J. Am. Chem Soc.* **1998,** *120*, 843-844.
25. Ferrere, S., *Chem. Mater.* **2000,** *12*, 1083-1089.
26. Ferrere, S., *Inorg. Chimica Acta* **2002,** *329*, 79-92.
27. Yang, M.; Thompson, D. W.; Meyer, G. J., *Inorg. Chem.* **2000,** *39*, 3738-3739.
28. Yang, M.; Thompson, D. W.; Meyer, G. J., *Inorg. Chem.* **2002,** *41*, 1254-1262.
29. Dixon, I. M.; Khan, S.; Alary, F.; Boggio-Pasqua, M.; Heully, J. L., *Dalt. Trans.* **2014,** *43*, 15898-15905.
30. Dixon, I. M.; Alary, F.; Boggio-Pasqua, M.; Heully, J.-L., *Dalt. Trans.* **2015,** *44*, 13498-13503.
31. Bessho, T.; Constable, E. C.; Graetzel, M.; Hernandez Redondo, A.; Housecroft, C. E.; Kylberg, W.; Nazeeruddin, M. K.; Neuburger, M.; Schaffner, S., *Chem. Commun.* **2008**, 3717-3719.
32. Housecroft, C. E.; Constable, E. C., *Chem. Soc. Rev.* **2015,** *44*, 8386-8398.
33. Bozic-Weber, B.; Constable, E. C.; Housecroft, C. E., *Coord Chem Rev* **2013,** *257*, 3089-3106.
34. McCusker, J. K.; Walda, K. N.; Dunn, R. C.; Simon, J. D.; Magde, D.; Hendrickson, D. N., *J. Am. Chem Soc.* **1993,** *115*, 298-307.

35. Monat, J. E.; McCusker, J. K., *J. Am. Chem Soc.* **2000,** *122*, 4092-4097.
36. Zhang, W.; Alonso-Mori, R.; Bergmann, U.; Bressler, C.; Chollet, M.; Galler, A.; Gawelda, W.; Hadt, R. G.; Hartsock, R. W.; Kroll, T.; Kjaer, K. S.; Kubicek, K.; Lemke, H. T.; Liang, H. W.; Meyer, D. A.; Nielsen, M. M.; Purser, C.; Robinson, J. S.; Solomon, E. I.; Sun, Z.; Sokaras, D.; van Driel, T. B.; Vanko, G.; Weng, T.-C.; Zhu, D.; Gaffney, K. J., *Nature* **2014,** *509*, 345-348.
37. Cammarata, M.; Bertoni, R.; Lorenc, M.; Cailleau, H.; Di Matteo, S.; Mauriac, C.; Matar, S. F.; Lemke, H.; Chollet, M.; Ravy, S.; Laulhé, C.; Létard, J.-F.; Collet, E., *Phys. Rev. Lett.* **2014,** *113*, 227402.
38. Auböck, G.; Chergui, M., *Nat Chem* **2015,** *7*, 629-633.
39. Jakubikova, E.; Bowman, D. N., *Acc Chem Res* **2015,** *48*, 1441-1449.
40. Vankó, G.; Bordage, A.; Pápai, M.; Haldrup, K.; Glatzel, P.; March, A. M.; Doumy, G.; Britz, A.; Galler, A.; Assefa, T.; Cabaret, D.; Juhin, A.; van Driel, T. B.; Kjær, K. S.; Dohn, A.; Møller, K. B.; Lemke, H. T.; Gallo, E.; Rovezzi, M.; Németh, Z.; Rozsályi, E.; Rozgonyi, T.; Uhlig, J.; Sundström, V.; Nielsen, M. M.; Young, L.; Southworth, S. H.; Bressler, C.; Gawelda, W., *J. Phys . Chem. C* **2015,** *119*, 5888-5902.
41. Van Kuiken, B. E.; Cho, H.; Hong, K.; Khalil, M.; Schoenlein, R. W.; Kim, T. K.; Huse, N., *J. Phys . Chem. Lett.* **2016,** *7*, 465-470.
42. Dixon, I. M.; Alary, F.; Boggio-Pasqua, M.; Heully, J.-L., *Inorg. Chem.* **2013,** *52*, 13369-13374.
43. Mukherjee, S.; Bowman, D. N.; Jakubikova, E., *Inorg. Chem.* **2015,** *54*, 560-569.
44. Dixon, I. M.; Boissard, G.; Whyte, H.; Alary, F.; Heully, J.-L., *Inorg. Chem.* **2016,** *55*, 5089-5091.
45. Jamula, L. L.; Brown, A. M.; Guo, D.; McCusker, J. K., *Inorg. Chem.* **2014,** *53*, 15-17.
46. Mengel, A. K. C.; Förster, C.; Breivogel, A.; Mack, K.; Ochsmann, J. R.; Laquai, F.; Ksenofontov, V.; Heinze, K., *Chem Eur. J.* **2015,** *21*, 704-714.
47. Liu, Y.; Harlang, T.; Canton, S. E.; Chabera, P.; Suarez-Alcantara, K.; Fleckhaus, A.; Vithanage, D. A.; Goransson, E.; Corani, A.; Lomoth, R.; Sundstrom, V.; Warnmark, K., *Chem. Commun.* **2013,** *49*, 6412-6414.
48. Fredin, L. A.; Pápai, M.; Rozsályi, E.; Vankó, G.; Wärnmark, K.; Sundström, V.; Persson, P., *J. Phys . Chem. Lett.* **2014,** *5*, 2066-2071.
49. Harlang, T. C. B.; Liu, Y.; Gordivska, O.; Fredin, L. A.; Ponseca Jr, C. S.; Huang, P.; Chábera, P.; Kjaer, K. S.; Mateos, H.; Uhlig, J.; Lomoth, R.; Wallenberg, R.; Styring, S.; Persson, P.; Sundström, V.; Wärnmark, K., *Nat Chem* **2015,** *7*, 883-889.
50. Liu, Y.; Kjær, K. S.; Fredin, L. A.; Chábera, P.; Harlang, T.; Canton, S. E.; Lidin, S.; Zhang, J.; Lomoth, R.; Bergquist, K.-E.; Persson, P.; Wärnmark, K.; Sundström, V., *Chem. Eur. J.* **2015,** *21*, 3628-3639.
51. Fredin, L. A.; Wärnmark, K.; Sundström, V.; Persson, P., *ChemSusChem* **2016,** *9*, 652-652.
52. Duchanois, T.; Etienne, T.; Cebrián, C.; Liu, L.; Monari, A.; Beley, M.; Assfeld, X.; Haacke, S.; Gros, P. C., *Eur. J. Inorg. Chem.* **2015,** *2015*, 2469-2477.
53. Duchanois, T.; Etienne, T.; Beley, M.; Assfeld, X.; Perpète, E. A.; Monari, A.; Gros, P. C., *Eur. J. Inorg. Chem.* **2014,** *2014*, 3747-3753.
54. Liu, L.; Duchanois, T.; Etienne, T.; Monari, A.; Beley, M.; Assfeld, X.; Haacke, S.; Gros, P. C., *Phy. Chem. Chem. Phys.* **2016,** *18*, 12550-12556.
55. Shepard, S. G.; Fatur, S. M.; Rappé, A. K.; Damrauer, N. H., *J. Am. Chem Soc.* **2016,** *138*, 2949-2952.
56. Liu, Y.; Persson, P.; Sundström, V.; Wärnmark, K., *Acc. Chem. Res.* **2016**.
57. Pastore, M.; De Angelis, F., *J. Am. Chem Soc.* **2015,** *137*, 5798-5809.
58. Kondov, I.; Čížek, M.; Benesch, C.; Wang, H.; Thoss, M., *J . Phys. Chem. C* **2007,** *111*, 11970–11981.
59. Sulzer, D.; Iuchi, S.; Yasuda, K., *J. Chem Theor. Comp.* **2016**.
60. Jiang, J.; Swierk, J. R.; Hedstrom, S.; Matula, A. J.; Crabtree, R. H.; Batista, V. S.; Schmuttenmaer, C. A.; Brudvig, G. W., *Phys . Chem. Chem. Phys.* **2016,** *18*, 18678-18682.
61. Pastore, M.; Angelis, F., Modeling Materials and Processes in Dye-Sensitized Solar Cells: Understanding the Mechanism, Improving the Efficiency. In *Top. Curr. Chem.*, Springer Berlin Heidelberg: 2014; pp 1-86.
62. Pastore, M.; Selloni, A.; Fantacci, S.; De Angelis, F., Electronic and Optical Properties of Dye-Sensitized TiO2 Interfaces. In *Top. Curr. Chem.*, Springer Berlin Heidelberg: 2014; pp 1-45.
63. Pápai, M.; Vankó, G.; Rozgonyi, T.; Penfold, T. J., *J. Phys. Chem. Lett.* **2016,** *7*, 2009-2014.
64. Lee, D. H.; Lee, M. J.; Song, H. M.; Song, B. J.; Seo, K. D.; Pastore, M.; Anselmi, C.; Fantacci, S.; De Angelis, F.; Nazeeruddin, M. K.; Gräetzel, M.; Kim, H. K., *Dyes Pigm.* **2011,** *91*, 192-198.
65. Jakubikova, E.; Snoeberger Iii, R. C.; Batista, V. S.; Martin, R. L.; Batista, E. R., *J. Phys. Chem. A* **2009,** *113*, 12532-12540.
66. Salvatori, P.; Amat, A.; Pastore, M.; Vitillaro, G.; Sudhakar, K.; Giribabu, L.; Soujanya, Y.; De Angelis, F., *Comp. Theor. Chem.* **2014,** *1030*, 59–66.

67. Agrawal, S.; Leijtens, T.; Ronca, E.; Pastore, M.; Snaith, H.; De Angelis, F., *J. Mater. Chem. A* **2013,** *1*, 14675-14685.
68. Umari, P.; Giacomazzi, L.; De Angelis, F.; Pastore, M.; Baroni, S., *J. Chem. Phys* **2013,** *139*, 014709-014709.
69. Galoppini, E., *Nat Chem* **2015,** *7*, 861-862.
70. Vittadini, A.; Selloni, A.; Rotzinger, F. P.; Grätzel, M., *Phy. Rev. Lett.* **1998,** *81*, 2954-2957.
71. Lundqvist, M. J.; Nilsing, M.; Persson, P.; Lunel, S., *Int. J. Quantum Chem.* **2006,** *106*, 3214-3234.
72. De Angelis, F.; Fantacci, S.; Mosconi, E.; Nazeeruddin, M. K.; Grätzel, M., *J . Phys. Chem. C* **2011,** *115*, 8825-8831.
73. te Velde, G.; Bickelhaupt, F. M.; Baerends, E. J.; Fonseca Guerra, C.; van Gisbergen, S. J. A.; Snijders, J. G.; Ziegler, T., *J. Comp. Chem.* **2001,** *22*, 931-967.
74. Becke, A. D., *Phys. Rev. A* **1988,** *38*, 3098-3100.
75. Perdew, J. P., ***Phys. Rev. B*** **1986,** *33*, 8822-8824.
76. Cossi, M.; Rega, N.; Scalmani, G.; Barone, V., *J. Comp. Chem.* **2003,** *24*, 669-681.
77. Barone, V.; Cossi, M., *The Journal of Physical Chemistry A* **1998,** *102*, 1995-2001.
78. Frisch, M. J.; Trucks, G. W.; Schlegel, H. B.; Scuseria, G. E.; Robb, M. A.; Cheeseman, J. R.; Scalmani, G.; Barone, V.; Mennucci, B.; Petersson, G. A.; Nakatsuji, H.; Caricato, M.; Li, X.; Hratchian, H. P.; Izmaylov, A. F.; Bloino, J.; Zheng, G.; Sonnenberg, J. L.; Hada, M.; Ehara, M.; Toyota, K.; Fukuda, R.; Hasegawa, J.; Ishida, M.; Nakajima, T.; Honda, Y.; Kitao, O.; Nakai, H.; Vreven, T.; Montgomery, J., J. A.; Peralta, J. E.; Ogliaro, F.; Bearpark, M.; Heyd, J. J.; Brothers, E.; Kudin, K. N.; Staroverov, V. N.; Kobayashi, R.; Normand, J.; Raghavachari, K.; Rendell, A.; Burant, J. C.; Iyengar, S. S.; Tomasi, J.; Cossi, M.; Rega, N.; Millam, N. J.; Klene, M.; Knox, J. E.; Cross, J. B.; Bakken, V.; Adamo, C.; Jaramillo, J.; Gomperts, R.; Stratmann, R. E.; Yazyev, O.; Austin, A. J.; Cammi, R.; Pomelli, C.; Ochterski, J. W.; Martin, R. L.; Morokuma, K.; Zakrzewski, V. G.; Voth, G. A.; Salvador, P.; Dannenberg, J. J.; Dapprich, S.; Daniels, A. D.; Farkas, Ö.; Foresman, J. B.; Ortiz, J. V.; Cioslowski, J.; Fox, D. J. *Gaussian 09*, Revision A.1; Gaussian, Inc.: Wallingford CT, 2009.
79. Muscat, J. P.; Newns, D. M., *Prog. Surf. Sci.* **1978,** *9*, 1-43.
80. Cohen-Tannoudji, C.; Diu, B.; Laloe, F., *Quantum Mechanics, Volume 2*. Wiley: 1977; p 1524.
81. Persson, P.; Lundqvist, M. J.; Ernstorfer, R.; Goddard, W. A.; Willig, F., *J. Chem. Theory Comput.* **2006,** *2*, 441-451.
82. Lundqvist, M. J.; Nilsing, M.; Lunell, S.; Åkermark, B.; Persson, P., *J. Phys Chem. B* **2006,** *110*, 20513-20525.
83. Persson, P.; Lundqvist, M. J., *J. Phys. Chem. B* **2005,** *109*, 11918-11924.
84. Persson, P.; Lunell, S.; Ojamäe, L., *Int. J. Quantum Chem.* **2002,** *89*, 172-180.
85. Ronca, E.; Marotta, G.; Pastore, M.; De Angelis, F., *J. Phys. Chem. C* **2014,** *118*, 16927-16940.
86. Kondov, I.; Čížek, M.; Benesch, C.; Wang, H.; Thoss, M., *J. Phys. Chem. C* **2007,** *111*, 11970-11981.
87. Li, J.; Wang, H.; Persson, P.; Thoss, M., *J. Chem. Phys.* **2012,** *137*, 22A529-516.
88. Barea, E. M.; Bisquert, J., *Langmuir* **2013,** *29*, 8773-8781.
89. O'Regan, B. C.; López-Duarte, I.; Martínez-Díaz, M. V.; Forneli, A.; Albero, J.; Morandeira, A.; Palomares, E.; Torres, T.; Durrant, J. R., *J. Am. Chem Soc.* **2008,** *130*, 2906-2907.
90. Altobello, S.; Argazzi, R.; Caramori, S.; Contado, C.; Da Fré, S.; Rubino, P.; Choné, C.; Larramona, G.; Bignozzi, C. A., *J. Am. Chem Soc.* **2005,** *127*, 15342-15343.
91. Wu, J.; Lan, Z.; Lin, J.; Huang, M.; Huang, Y.; Fan, L.; Luo, G., *Chem. Rev.* **2015,** *115*, 2136-2173.
92. Pastore, M.; Etienne, T.; De Angelis, F., *J. Mater. Chem. C* **2016,** *4*, 4346-4373.